

# Electronic, magnetic, and structural properties of the ferrimagnet $\text{Mn}_2\text{CoSn}$

Jürgen Winterlik, Gerhard H. Fecher, Benjamin Balke, Tanja Graf, Vajiheh Alijani,  
Vadim Ksenofontov, Catherine A. Jenkins<sup>1</sup>, Olga Meshcheriakova, and Claudia Felser\*

*Institute for Inorganic and Analytical Chemistry,  
Johannes Gutenberg University Mainz, D-55128, Germany*

<sup>1</sup>*present address: Advanced Light Source, Lawrence Berkeley National Laboratory, Berkeley, CA and*

*\* author to whom correspondence should be addressed: felser@uni-mainz.de*

Guodong Liu

*School of Materials Science and Engineering, Hebei University of Technology, Tianjin 300130, China*

Shigenori Ueda and Keisuke Kobayashi

*National Institute for Materials Science, 1-1-1 Kouto, Sayo-cho, Sayo-gun, Hyogo 679-5198, Japan*

Tetsuya Nakamura

*JASRI, 1-1-1 Kouto, Sayo-cho, Sayo-gun, Hyogo 679-5198, Japan*

Marek Wójcik

*Polish Academy of Sciences, Aleja Lotnikow 32/46, 02-668, Warszawa, Poland*

(Dated: 22 February 2011)

The magnetic ground state of the Heusler compound  $\text{Mn}_2\text{CoSn}$  was predicted to be nearly half-metallic ferrimagnetic with a high spin polarization by *ab initio* electronic structure calculations.  $\text{Mn}_2\text{CoSn}$  was synthesized, and the magnetic behavior of the compound was studied using SQUID magnetometry and x-ray magnetic circular dichroism. The experimental values were found to be in fair accordance with the theoretical predictions. The electronic structure and the crystal structure of  $\text{Mn}_2\text{CoSn}$  were characterized comprehensively using x-ray powder diffraction,  $^{119}\text{Sn}$  Mössbauer spectroscopy, nuclear magnetic resonance, and hard x-ray photoelectron spectroscopy.

## LBNL Disclaimer

This document was prepared as an account of work sponsored by the U.S. Government. While this document is believed to contain correct information, neither the U.S. Government nor any agency thereof, nor the Regents of the University of California, nor any of their employees, makes any warranty, express or implied, or assumes any legal responsibility for the accuracy, completeness, or usefulness of any information, apparatus, product, or process disclosed, or represents that its use would not infringe privately owned rights. Reference herein to any specific commercial product, process, or service by its trade name, trademark, manufacturer, or otherwise, does not necessarily constitute or imply its endorsement, recommendation, or favoring by the U.S. Government or any agency thereof, or the Regents of the University of California. The views and opinions of authors expressed herein do not necessarily state or reflect those of the U.S. Government or any agency thereof or the Regents of the University of California.

## I. INTRODUCTION

The history of ternary intermetallic Heusler compounds began in the year 1903 when F. Heusler reported on archetypical  $\text{Cu}_2\text{MnAl}$  [1]. This compound is the classic example of a ferromagnet that does not contain any ferromagnetic element. Heusler compounds exhibit the stoichiometric composition  $\text{X}_2\text{YZ}$  and crystallize in the cubic  $\text{L2}_1$  structure (space group 225,  $Fm\bar{3}m$ ). This structure consists of four interpenetrating fcc lattices. The related  $\text{CuHg}_2\text{Ti}$  ( $X_a$ ) structure (space group 216,  $F\bar{4}3m$ ) is referred to as an inverse Heusler structure and differs from the  $\text{L2}_1$  structure in that different atoms occupy the tetrahedrally coordinated lattice sites. The stoichiometry changes to  $\text{XX'YZ}$  and the Wyckoff position  $8c$  splits into  $4c$  and  $4d$  thereby reducing the symmetry and removing the center of inversion. This modification occurs in the majority of cases when the  $Y$  atom of a Heusler compound is more electronegative than the atoms  $X_2$ .

Heusler compounds show strong  $d$ -electron-mediated electronic properties resulting in a multitude of different applications. The magnetic properties of Heusler compounds include a large variety of interesting phenomena beginning with metallic ferromagnetism as in the case of the aforementioned  $\text{Cu}_2\text{MnAl}$ . The half-metallic ferromagnets such as  $\text{Co}_2\text{MnSi}$  [2,3] are metallic only in one spin channel while the opposite spin channel exhibits an insulating or semi-conducting band structure. This type of material is highly relevant for spintronics applications [4]. Several Heusler compounds were reported to become superconducting [5-7] others show magnetic shape memory [8,9] magnetocaloric [10,11] or thermoelectric effects [12,13]. Only one Heusler compound was found to exhibit an antiferromagnetic type of magnetic order [14].

The ferrimagnets  $\text{Mn}_2\text{YZ}$  are an especially interesting class within the Heusler family.  $\text{Mn}_3\text{Ga}$  belongs to this class and one of its phases crystallizes in a tetragonally distorted variation of the Heusler cell (space group 139,  $I4/mmm$ ) [15-17]. Its relatively low magnetic moment in combination with the high Curie temperature  $T_C$  and high spin polarization make tetragonal  $\text{Mn}_3\text{Ga}$  attractive for implementation in spin torque transfer magnetic random access memory (STT-MRAM) devices [18-20]. The desired properties of the materials  $\text{Mn}_{3-x}\text{Ga}$  can easily be tuned by substitution of elements, *i.e.*, variation of the Mn:Ga ratio. The recently discovered ferrimagnetic shape memory compound  $\text{Mn}_2\text{NiGa}$  exhibits a record-breaking magnetic-field-induced strain of approximately 21% in its single crystalline form [21,22].  $\text{Co}_2$ -based Heusler compounds often follow the Slater-Pauling rule, which is a signature for their half metallicity. In the context of spintronics applications it is important to check whether the  $\text{Mn}_2$ -based Heusler compounds behave in a similar way. However, the situation in the  $\text{Mn}_2$ -based compounds is expected to be more complex because of different magnetic coupling and electronic correlations, which may be important due to highly localized magnetic moments of Mn atoms in the octahedral environment [23].

In this work we present results of a detailed theoretical and experimental investigation (structure and magnetic properties) of ferrimagnetic  $\text{Mn}_2\text{CoSn}$ , which is isoelectronic to  $\text{Mn}_2\text{NiGa}$ . Experiments on  $\text{Mn}_2\text{CoSn}$  were previously reported by different groups [24-27]. According to Ref. 27, ordered  $\text{Mn}_2\text{CoSn}$  should crystallize in the inverse cubic Heusler structure with three different magnetic sublattices as depicted in Fig. 1. In this structure the appearance of Mn-Mn nearest neighbors allows for the antiparallel coupling of the magnetic moments at the two different sites occupied by Mn leading to ferrimagnetic configurations. From the experimental investigations of the crystal structure,

however, L2<sub>1b</sub>-type disorder between Mn and Co in the tetrahedral surroundings of the cell was deduced. The calculated electronic structure is in accordance with this finding and suggests a nearly half-metallic band structure with a high spin polarization at the Fermi level for the L2<sub>1b</sub> disordered cell of Mn<sub>2</sub>CoSn making it attractive for spintronics.

## II. EXPERIMENTAL DETAILS

Polycrystalline ingots of Mn<sub>2</sub>CoSn were prepared by repeated arc melting of stoichiometric mixtures of the elements in an argon atmosphere to avoid oxygen contamination. The samples were subsequently annealed for two weeks at 1073 K in evacuated quartz tubes. After the annealing process, the samples were quenched to 273 K in a mixture of ice and water to retain the desired  $F\bar{4}3m$  structure. Slow cooling of the samples after the annealing process can lead to structural inhomogeneity [28].

For x-ray powder diffraction (XRD), a part of the sample was ground to a fine powder. The XRD measurements were carried out at room temperature using a Seifert XRD 3003 PTS diffractometer equipped with a Cu K $\alpha$  x-ray tube.

The magnetic properties were investigated using a superconducting quantum interference device (SQUID, Quantum Design MPMS-XL-5). Small, nearly spherical pieces of the samples with a weight of  $\sim 45$  mg were used in these measurements.

For the hard x-ray photoemission spectroscopy (HAXPES) and x-ray magnetic circular dichroism (XMCD) investigations, the samples were fractured *in situ* ensuring that the samples are free of oxygen contamination. The HAXPES experiments were performed at the beamline BL15XU of SPring-8 (Japan). The photon energy was fixed at 5.9534 keV using a double crystal monochromator and a Si 333 channel-cut monochromator. The photoemitted electrons were analyzed for their kinetic energy and detected by means of a hemispherical analyzer (VG Scienta R4000). The overall energy resolution (monochromator plus analyzer) was set to 250 meV, as verified by spectra of the Au valence band at the Fermi energy ( $\epsilon_F$ ). The angle between the electron spectrometer and photon propagation is fixed at 90°. The photons are *p* polarized; i.e., the electric field vector is in the plane of incidence and always points in the direction of the electron detector. A near normal emission ( $\theta = 8^\circ$ ) detection angle was used. This corresponds to an angle of incidence of  $\alpha = \theta - 90^\circ = 82^\circ$ . Note that the angles are not well defined for the cleaved bulk samples due to surface roughness.

The XMCD measurements were performed using the magnetic circular dichroism measurement system at the BL25SU [29,30] beamline of SPring-8. The helicity switching of the circularly polarized radiation is performed by twin helical undulators. The frequency of switching was 1 Hz. The two absorption spectra required to determine the XMCD were measured by one energy scan switching the helicity at each energy point. To minimize systematic errors, the XMCD spectrum was measured at +1.9 T and -1.9 T, respectively. The absorption signal was measured in the total electron yield mode with the energy resolution set to  $E/\Delta E = 5 \cdot 10^3$ . The samples were magnetized in an induction field of  $\mu_0 H = \pm 1.9$  T by a water-cooled electromagnet. The sample temperature was set to 15 K.

The hyperfine magnetic fields at the Co, Mn, and Sn sites were determined by nuclear magnetic resonance (NMR)

and  $^{119}\text{Sn}$  Mössbauer spectroscopy. Mössbauer spectroscopy was performed using a constant-acceleration spectrometer at 225 K in transmission geometry. For excitation, a  $^{119}\text{Sn}(\text{CaSnO}_3)$  source was used delivering  $\gamma$  radiation with an energy of  $h\nu = 23.9$  keV. The intrinsic linewidth of the source is  $\Delta\nu = 0.3235$  mm/s. Sn with a natural abundance of 8.6%  $^{119}\text{Sn}$  was used for the samples of the present study. The analysis of the Mössbauer data was performed using the RECOIL software package [31]. The NMR experiments were performed in an automated, coherent, spin-echo spectrometer at 4.2 K [32]. The NMR spectra were recorded in the frequency range of 20-400 MHz in steps of 2 MHz to ensure that both signals from  $^{55}\text{Mn}$  and  $^{59}\text{Co}$  are in the range of the spectra. The measurements were performed without applying an external magnetic field. All NMR spectra were corrected regarding the enhancement factor as well as the  $\nu^2$  dependence, resulting in relative intensities proportional to the number of nuclei with a given NMR resonance frequency.

### III. COMPUTATIONAL DETAILS

The basic electronic structure calculation and the optimization of the lattice parameter were carried out using the scalar-relativistic full potential linearized augmented plane wave method (FLAPW) as provided by WIEN2K [33]. The exchange-correlation functional was taken within the generalized gradient approximation (GGA) in the parametrization of Perdew- Burke-Ernzerhof (PBE) [34]. For comparison, LDA + $U$  was used to account for electronic correlations in the localized moment system [35]. LDA + $U$ , as described by Anisimov et al. [36], adds an orbital-dependent electron-electron correlation, which is not included in the plain LSDA or GGA schemes. In particular, the LDA + $U$  self-interaction correction scheme (SIC) [37] was used here to account for double-counting corrections. Further use was made of  $J = 0$  and  $U_{eff} = U - J(U = F^0)$ . The use of  $U_{eff} = U - J$  suppresses multipole effects. This means, it neglects the nonspherical terms in the expansion of the Coulomb interaction. This choice does not affect the results presented here, as  $U$  was used in a parametric way. The values of  $U_{eff}$  were set to  $U_{Co} = 0.14$  Ry and  $U_{Mn} = 0.12$  Ry for both the different lattice sites of Mn atoms in the cell. It should be mentioned that the + $U$  was used in the FLAPW scheme with the GGA rather than the LSDA parametrization of the exchange-correlation functional. No significant differences were observed using either of the parametrizations. A basic  $31 \times 31 \times 31$  mesh was used for integration. This results in 816  $k$  points in the irreducible wedge of the Brillouin zone of the primitive cell. The number of plane waves was restricted by  $Rk_{max} = 7$ . Both total energy ( $10^{-5}$  Ry) and charge ( $10^{-2}e^-$ ) were used simultaneously as criteria for convergence.

Further electronic structure calculations have been carried out using the full relativistic spin-polarized Korringa-Kohn- Rostocker method (SPR-KKR) provided by Ebert et al [38-40]. This program provides the coherent potential approximation (CPA) for calculating the properties of alloy systems with random distribution of the atoms. The SPR-KKR calculations have been performed using the PBE generalized gradient approximation (GGA) [34]. The CPA tolerance was set to  $10^{-4}$  and the energy convergence criterion to  $10^{-5}$ .  $f$  states were included in the basis of all atoms. 832 irreducible  $k$  points based on a  $22 \times 22 \times 22$  mesh have been used for integration. The density of states is calculated for the double number of  $k$  points from the Greens function by adding a small imaginary part of 0.002 Ry to the energy. For smaller values, the band gaps may become better visible; however, at the same time the

DOS becomes much more noisy.

## IV. RESULTS AND DISCUSSION

### A. Structural properties

The crystal structure of annealed and quenched  $\text{Mn}_2\text{CoSn}$  was determined using powder XRD with  $\text{Cu K}\alpha$  radiation. The diffraction pattern is shown in Fig. 2. It reveals the inverse cubic Heusler structure of  $\text{Mn}_2\text{CoSn}$ . A small impurity phase is found in the diffraction pattern. This phase was identified to be tetragonal  $\text{MnSn}_2$  (space group 140,  $I4/mcm$ ) [41]. The amount of impurity is obviously very small. A Rietveld refinement of the experimental data was performed using the TOPAS ACADEMIC software package [42]. The cubic lattice parameter was determined to be  $a = (6.083 \pm 0.002) \text{ \AA}$ . The Rietveld figures of merit for the inverse Heusler structure are  $R_{\text{Bragg}} = 3.59\%$ ,  $R_{\text{wp}} = 25.15\%$ . The low  $R_{\text{Bragg}}$  value clearly indicates that the structural model is accurate;  $R_{\text{wp}}$  is large due to the impurity, which was calculated to amount to approximately 5%8%. The determination of order/disorder in  $\text{Mn}_2\text{CoSn}$  by powder XRD poses difficulties due to similar scattering factors of Mn and Co. An admixture of Mn atoms on the Co position and vice versa corresponding to a  $\text{L}_{21b}$ -type or even  $\text{DO}_3$ -type disorder can thus not be excluded. In  $\text{DO}_3$  the transition metals (here: Mn, Co) commonly share the  $8c$  and  $4b$  positions of the fcc cell with  $Fm\bar{3}m$  symmetry while the main group element (here: Sn) exclusively occupies the  $4a$  position. A  $\text{DO}_3$ -type disorder is, however, implausible because Mn atoms generally prefer the octahedrally surrounded position in the Heusler cell, especially when the more electronegative Co atoms are present. An  $\text{L}_{21b}$  disorder as currently reported for related systems [43] is possible. An  $\text{L}_{21b}$  type structure was previously reported for  $\text{Mn}_2\text{NiSn}$  [44] and recently also confirmed for  $\text{Mn}_2\text{NiGa}$  by neutron diffraction experiments [45]. In this structure type, the  $8c$  position of the fcc cell with  $Fm\bar{3}m$  symmetry is equally populated by Ni and Mn atoms, whereas the  $4b$  and  $4a$  positions are exclusively occupied by Mn and the main group element (Sn, Ga), respectively. It is furthermore evident from the Rietveld refinement and the relative intensities of the (111) and (200) reflections that the Sn atoms do not mix with Co or Mn.

### B. First-principles calculations of the electronic structure

$\text{Mn}_2\text{CoSn}$  has 27 valence electrons, and therefore we expect from the Slater-Pauling rule a magnetic moment of  $3 \mu_B$  for half-metallicity. However, to understand this complex magnetic material in detail we have calculated the electronic structure and the magnetic properties. Before calculating details of the electronic structure, a geometry optimization of the  $\text{CuHg}_2\text{Ti}$  structure was performed using WIEN2K. The optimization resulted in two different minima of the total energy as a function of the cell volume as shown in Fig. 3. One of the states is a half-metallic ferrimagnet (HMF) and the other one a regular ferrimagnet (FiM). The difference in the total energies of these two states is only 14 meV.

An equation-of-states fit resulted in a relaxed lattice parameter of  $a_{\text{HMF}} = 6.034 \text{ \AA}$  and a bulk modulus of  $B = 128 \text{ GPa}$  for the half-metallic state. The state with lower total energy is the ferrimagnetic state with a slightly larger lattice parameter of  $a_{\text{FiM}} = 6.080 \text{ \AA}$  and a smaller bulk modulus of  $B = 113 \text{ GPa}$ . For lattice parameters below

5.98 Å no stable convergence was reached for the ferrimagnetic solution. Similarly, the half-metallic state was not stable above 6.06 Å. In both cases the charge convergence criterion ( $0.001 e^-$ ) was hardly reached, if at all. The corresponding magnetic moments are included as open symbols in Fig. 3(b).

Details of the electronic structure were calculated for both states. Figures 4 and 5 display the calculated band structure and density of states of HMF and regular FiM states, respectively. The HMF (Fig. 4) exhibits for the minority electrons a small band gap at the Fermi energy with a width of approximately 190 meV. In the FiM state (Fig. 5), this gap is closed and the corresponding minimum in the density of states is shifted below the Fermi energy. Overall, the differences between the electronic structures are only very small. Even though the differences between the electronic structures of the HMF and FiM states are only very small, they have a high impact on the magnetic properties. Table I shows the calculated local and total magnetic moments of  $\text{Mn}_2\text{CoSn}$  using the GGA and the LDA +  $U$  for both ground states HMF and FiM. In all cases the magnetic moments at the Mn I atoms are antiparallel to those of the Mn II atoms resulting in the ferrimagnetic order. The total magnetic moment in the FiM state is considerably lower as compared to the HMF state.

To avoid misinterpretation that may be caused by the particular computational method additional calculations were performed using the SPR-KKR method. Depending on the initial settings for the magnetization, it turned out that the calculations do not converge unambiguously into a definite ground state. Similar problems were recently reported for  $\text{Mn}_2\text{CoIn}$  and  $\text{Mn}_2\text{CoSn}$  [43]. Meinert et al. had to reduce the lattice parameters in order to find a ground state. In the present study, it was possible to stabilize the ferrimagnetic ground state at 6.05 Å and slightly above and the half-metallic ground state below 6.04 Å. In all other cases, the calculations did not converge due to fluctuating magnitude of the magnetic moments, or converged into the opposite ground state, dependent on the lattice parameter but independent of the initial parameters for the magnetization. This demonstrates again that the calculated magnetic ground state is not stable in the  $X_a$ -type structure.

A different structure was suggested for the related Heusler compound  $\text{Mn}_2\text{NiGa}$  by Brown et al [45]. Based on neutron diffraction, Brown et al. reported an  $\text{L2}_{1b}$ -type structure in the cubic phase. This is a disordered type of  $X_2YZ$  regular Heusler compounds ( $\text{L2}_{1a}$ ) and has also  $Fm\bar{3}m$  symmetry. In this structure, the transition metals  $X$  and  $Y$  occupy simultaneously the  $8c$  Wyckoff position by 50% each, the remaining part of the  $X$  atoms occupies  $4b$ , and the main group element  $Z$  occupies  $4a$ . Different from the  $X_a$  structure,  $\text{L2}_{1b}$  has a center of inversion as the regular Heusler compounds. CPA calculations that account for the Mn-Co disorder on the  $8c$  positions were carried out in addition. Other than the calculations for the  $X_a$  structure, these calculations converged unambiguously into a definite ground state.

Figure 6 compares the spin density of states of  $\text{Mn}_2\text{CoSn}$  for the different magnetic and structural states as calculated by the fully relativistic SPR-KKR method. The gap in the minority states of the HMF state is not resolved because its width is only 190 meV, which is in the order of the Lorentzian broadening used in the calculation. Comparing the density of states of the HMF and FiM states [Figs. 6(a) and 6(b)], the magnetic instability observed in the calculations becomes clear. In the HMF state, there is a maximum of the density of states at the Fermi energy in the majority channel, whereas a maximum of the density of states at the Fermi energy appears in the minority channel of the FiM

state. These maxima are not compensated in the opposite spin channels and lead to a maximum in the total density of states. Such a maximum does not appear in the  $L2_{1b}$  structure, and therefore it becomes structurally more stable. It is interesting to note that the electronic structure of the  $L2_{1b}$  structure exhibits a high spin polarization at the Fermi energy and is very close to a half-metallic state. This half-metallic state cannot be unambiguously substantiated, however, due to the missing periodicity and loss of the band structure in the structure with random occupation of sites.

Table II compares the magnetic moments for the different ground states and structures as calculated by SPR-KKR. As mentioned above, in the  $X_a$  structure the total magnetic moment and the moment of Mn I depend strongly on the lattice parameter.

### C. Mössbauer and NMR spectroscopy

The results of the Sn Mössbauer experiments are displayed in Fig. 7. The spectra were taken at 225 K in transmission mode. It is obvious that the spectra are composed of several subspectra. Spectrum (I) corresponds to an as-cast sample from the arc melter. It exhibits a clear magnetic hyperfine splitting. A small additional line with much smaller splitting appears in the center of spectrum (II), which corresponds to an annealed and quenched sample of  $Mn_2CoSn$ .

The fit of the spectra of the as-cast sample (I) requires at least four different species with hyperfine magnetic fields of  $H_{hf}^{IA} = 250$  kOe,  $H_{hf}^{IB} = 180$  kOe,  $H_{hf}^{IC} = 150$  kOe,  $H_{hf}^{ID} = 119$  kOe and relative intensities of 65%, 18%, 8%, and 9%. The first subspectrum (IA) has a broad unresolved structure with a linewidth of 4.3 mm/s, which is essentially larger than the natural linewidth of the source. The linewidths of the remaining three subspectra are approximately 1.3 mm/s. The average value of the isomer shift for all four subspectra is 1.74 mm/s relative to  $CaSnO_3$ . After annealing, the structure of the Mössbauer spectrum becomes more pronounced, and a weak subspectrum with a relative intensity of 3% and much smaller hyperfine splitting appears in the central part of the spectrum (II). The isomer shift of this subspectrum is 1.9 mm/s. The low hyperfine field ( $H_{hf}^{I0} = 15$  kOe) indicates a distinct position of the Sn atoms. Different from the as-cast sample, a reasonable fit of the spectrum of sample II requires three additional magnetic subspectra with hyperfine fields of  $H_{hf}^{IIA} = 238$  kOe,  $H_{hf}^{IIB} = 171$  kOe, and  $H_{hf}^{IIE} = 123$  kOe and relative intensities of 58%, 20%, and 19%, respectively. Subspectrum IIA of the annealed sample with a broad unresolved structure corresponds to the subspectrum IA of the as-cast sample but has a reduced contribution. Similarly, IB and IIB correspond to each other, with a slightly higher contribution of IIB. A correspondence between subspectra IC, ID, and IIE is, however, not clear due to the low contributions.

The hyperfine magnetic fields experienced by the tin atoms are completely induced by the surrounding magnetic dipoles because they do not carry a magnetic moment. The appearance of a weak magnetic site (II0) in the spectrum of the annealed sample indicates a diffusion of the tin atoms to sites having a much weaker magnetic environment. The low value of the hyperfine field thus may be due to diffusion of Sn to grain boundaries or other crystal defects.

Figure 8 displays the result from the NMR investigation. The spectrum was taken from the annealed sample used in the Mössbauer experiments. The spectrum exhibits two distinct maxima at frequencies of  $\nu_1 = 79.4$  MHz and  $\nu_2 = 138.6$  MHz arising from the hyperfine fields at the Mn and Co sites. Further, broad features are detected in the

high-frequency part of the spectrum with weakly resolved maxima at 181 MHz, 200 MHz, and 246 MHz (see fit in Fig. 8). The broad distribution in the frequency range between 170 MHz and 330 MHz should correspond to Mn II atoms in different surroundings. Due to the equivalence in the first coordination sphere of Sn and Mn II atoms in the structure of  $\text{Mn}_2\text{CoSn}$ , a broadly distributed structure of NMR signals of Mn II atoms clearly correlates with the  $^{119}\text{Sn}$  Mössbauer magnetic subspectra. It is therefore possible to apply the results of Mössbauer spectroscopy to fit the Mn II part of the NMR spectrum of sample II. The deconvolution of the complete spectrum was performed using Gaussian peaks. The spectrum was decomposed into three groups of lines that correspond to Mn I, Co, and Mn II with an intensity ratio close to 1 : 1 : 1. The fit of the Mn II signal was done using three resonance lines. During the fit their relative intensities were kept equal to the relative intensities of lines IIAIC taken from the Mössbauer experiment. The results of the deconvolution are shown in Table III.

The comparison of NMR and Mössbauer measurements allows the conclusion that the species with the lowest  $H_{hf}$  and narrowest signals in the  $^{59}\text{Mn}$  II NMR and  $^{119}\text{Sn}$  Mössbauer spectra correspond to a stoichiometric local surrounding of Mn II and Sn atoms in  $\text{Mn}_2\text{CoSn}$  comprising 4 Co and 4 Mn I atoms. The relative intensity of 19% of the corresponding NMR signal at 181 MHz and the Mössbauer subspectrum with  $H_{hf}^{IIC} = 123$  kOe indicates that even the annealed sample II cannot be classified as well ordered. Substitution of Co with Mn I atoms and vice versa leads to an imbalance of magnetic moments and, consequently, to an increase of the effective  $H_{hf}$  on the Sn and Mn II atoms. Accordingly, one should attribute the NMR resonance line at 200 MHz and the Mössbauer subspectrum with  $H_{hf}^{IIB} = 171$  kOe to Mn II and Sn atoms having 3 Co + 5 Mn I or 5 Co + 3 Mn I neighbors in the first coordination sphere. The very broad NMR line centered at 246 MHz and the broad unresolved Mössbauer subspectrum with  $H_{hf}^{IIA} = 238$  kOe and a relative intensity of 58% stems from the scope of rest configurations  $(4 - n)\text{Co} + (4 + n)\text{Mn I} / (4 + n)\text{Co} + (4 - n)\text{Mn I}$  with  $n = 2, 3, 4$ . The impurity phase  $\text{MnSn}_2$ , which was detected in the diffraction pattern of  $\text{Mn}_2\text{CoSn}$ , was not found in the Mössbauer measurement. This may be due to the detection limit of this experimental setup, which amounts to approximately 3%. A fluctuation of the impurity content in different regions of the sample occurs inherently in polycrystalline intermetallic samples, and the powder taken for the the Mössbauer measurement may have had a lower content of  $\text{MnSn}_2$  as compared to the XRD sample, where an impurity concentration of 5%-8% was determined.

In summary, it follows from the NMR and Mössbauer spectroscopic data that antisite disorder between Co and Mn I is favored in  $\text{Mn}_2\text{CoSn}$  corresponding to the aforementioned  $\text{L2}_{1b}$ -type structure. From the NMR studies it can also be deduced that Mn II atoms are likely to be less subject to antisite disorder. This conclusion is based on the absence of the hyperfine structure in the NMR signal of Mn I. The signal at 79.4 MHz is relatively narrow and indicates no antisite disorder in the first coordination sphere of Mn I comprising four Sn and four Mn II atoms. Similar considerations can be applied to interpret the  $^{59}\text{Co}$  NMR signal at 138.6 MHz. The effects of the second coordination spheres of Co and Mn I comprising 6 Mn I and 6 Co atoms, respectively, are rather weak and are not seen in the NMR signals.



### D. Hard x-ray photoelectron spectroscopy

Figure 9 displays the results of the core-level photoemission from  $\text{Mn}_2\text{CoSn}$  excited by hard x-rays of approximately 6 keV energy. Typical states of the contributing elements were selected that exhibit a clearly detectable spin-orbit splitting.

The Mn  $2p_{3/2}$  state has a typical multiplet structure with a splitting of 1 eV. This splitting is not revealed at the Mn  $2p_{1/2}$  state but leads only to a considerable broadening of the line. Additional, weaker satellites show up at about 4 eV and 7 eV below the Mn  $2p_{3/2}$  and  $2p_{1/2}$  states, respectively. The multiplet splitting of the Mn  $2p$  states arises from the interaction of the core-hole with the partially filled d bands that are strongly localized [46,47]. The Co  $2p_{3/2}$  state exhibits a sharp satellite at about 3.49 eV below the maximum. This satellite is only weakly seen at the Co  $2p_{1/2}$  state. The Co satellite may be due to a shake-up transition from states just below the Fermi energy into the onset of the unoccupied s bands seen in Figs. 4, 5, and 6 at about 3-4 eV above the Fermi energy  $\epsilon_F$ . An influence of the interaction between the core-hole with the partially filled d bands, however, cannot be excluded.

The spin-orbit splittings of the core level are summarized in Table IV. The experimental values are compared to the calculations for  $\text{Mn}_2\text{CoSn}$ . The calculated values did not depend on the type of magnetic order; only small shifts in the binding energies were found that are below the experimental resolution. No differences are observed if comparing the calculational methods. The observed and calculated values for Co and Sn are in good agreement. A considerable deviation is found for the Mn  $2p$  states (about 1 eV). The reason is the observed multiplet splitting that is not accounted for in the calculations. The interaction between the core-hole and valence electrons in the photoexcited state causes an additional increase of the splitting on top of the ground-state spin-orbit interaction.

Figure 10 compares the valence band photoelectron spectra and the calculated total density of states  $[n(E)]$  of  $\text{Mn}_2\text{CoSn}$ . For better comparison, the density of states is convoluted by a Fermi-Dirac distribution ( $T = 300$  K) and smoothed by a Gaussian with a width of 250 meV. The latter accounts for the experimental resolution but neglects, however, any broadening caused by lifetime effects. The photoelectron spectra were taken at room temperature using an excitation energy of about 6 keV. It was previously demonstrated that the cross section of the contributing states ( $s$ ,  $p$ , and  $d$ ) are nearly equal at this photon energy [3]. This allows easily a direct comparison of the photoelectron spectra and the calculated density of states.

The comparison between the measured valence band spectra and the calculated total density of states reveals that  $n(E)$  is well described in the GGA approach. In particular the first maximum of the spectrum at about -1.3 eV below  $\epsilon_F$  corresponds to the maximum of  $n(E)$ . The second maximum appears in  $n(E)$  at about -2.9 eV. Further, the  $s - p$  hybridization gap at around -7 eV to -8 eV is clearly revealed in the photoelectron spectrum. LDA + $U$  (not shown here) results in shifts of the main features away from the Fermi energy, which is not compatible with the photoelectron spectra.

The differences in the density of states of the two different ground states of the  $X_a$  structure are too small to be distinguished in the photoelectron spectra, and also the main features are not much different from  $\text{L2}_{1b}$ . However, from  $n(E)$  there is a clear difference between the  $\text{L2}_{1b}$  and the  $X_a$  structures. In the latter structures an enhanced intensity is expected at the Fermi energy that is clearly absent in the valence band photoelectron spectrum. This

observation gives a clear advice that the investigated sample has the  $L2_{1b}$  structure.

## E. Magnetic properties

### 1. SQUID

The magnetic properties of the polycrystalline annealed and quenched sample were investigated by means of SQUID magnetometry. The field-dependent magnetic moments at different temperatures are displayed in Fig. 11. The saturation moment amounts to  $m_0 = 2.59 \pm 0.2 \mu_B$  at  $T = 5$  K. The large error is due to the impurity  $MnSn_2$  found in the XRD pattern. It is obvious that the material exhibits a small irreversible part in the hysteresis loop at 5 K as known for soft ferrimagnets. The inset of Fig. 11 shows the temperature-dependent magnetic moment of  $Mn_2CoSn$ . The Curie temperature of the compound was determined to be  $T_C = 598 \pm 5$  K. This Curie temperature allows for applications far beyond room temperature. From the Slater-Pauling curve  $3 \mu_B$  would be expected for the half-metallic ferrimagnetic ground state (HMF) while the calculations predicted  $1.74 \mu_B$  (GGA) and  $2.15 \mu_B$  (LDA+ $U$ ) for the ferrimagnet, and nearly half-metallic  $2.98 \mu_B$  for the proposed  $L2_{1b}$  disorder (see Table V). The experimental value lies in between these values but much more in the vicinity of the half-metallic states. As the impurity may be subject to lowering the magnetic moment rather than increasing it and the measurement temperature was 5 K while the calculations are based on 0 K, a nearly half-metallic ferrimagnetic state of  $Mn_2CoSn$  with a high spin polarization is most likely.

### 2. X-ray absorption and XMCD

The results of the photoabsorption measurements are shown in Fig. 12. Both elements, Mn and Co, exhibit typical metallic-like white lines at the  $L_{3,2}$  absorption edges. In particular, the Mn-derived spectra do not show an additional splitting. An additional peak appears in the Co spectrum at 3.36 eV above the maximum of the  $L_3$  line [marked by an arrow in Fig. 12(c)]. Its energy corresponds to the one observed in the HAXPES core-level spectra (see Sec. IVD). This feature is typical for materials with the fcc lattice [48]. It arises from a transition into  $s-p$  hybridized unoccupied states and exhibits no XMCD. It is also observed in other well-ordered Heusler compounds [49].

From the maximum intensities at the  $L_{3,2}$  edges spin-orbit splittings of  $\Delta_{SO}^{Mn} = 11.4$  eV and  $\Delta_{SO}^{Co} = 15.2$  eV for the initial  $2p$  states of Mn and Co, respectively, are determined. As expected, the values coincide with those of the HAXPES study (see Sec. IVD and Table IV).

Neither the intensity nor the XMCD at the Mn  $L_3$  edge hint directly at different magnetic sites. However, a small saddle point is observed 1.2 eV before the maximum of the XMCD at the Mn  $L_2$  edge that may indicate different sites. The XMCD signal of the Co  $L_{3,2}$  edges exhibits a clear splitting. It is seen as broadening of the XMCD signal at the  $L_2$  edge. It is clearly detectable at the  $L_3$  edge and amounts to about 1.3 eV. This splitting may be caused either by correlation effects or by different Co sites. It has to be noted that this structure is obviously not related to the above-mentioned structural feature of the Co absorption spectrum. The XMCD signal of both elements, Co and Mn, has the same sign being evident for a parallel coupling of the magnetic moments. It means that the Co spin

moments couple parallel to Mn II in the 4b position with the higher absolute spin moment. This is in agreement with the calculations.

According to a sum-rule analysis the spin magnetic moment at the Mn site amounts to  $m_{Mn} = 0.84\mu_B$  assuming five  $d$  holes. This value has to be compared to the average value  $m_{Mn} = (m_{MnI} + m_{MnII})/2$  due to the partial compensation of the moments. The orbital to spin moment ratio is found to be  $m_l/m_s = 0.045$ . However, this is only a rough estimate as it is also influenced by the overlapping intensities of the Mn I and Mn II atoms. Analyzing the Co spectrum it is found that  $m_{Co} = 0.72\mu_B$  and  $m_l/m_s = 0.078$  assuming three  $d$  holes. This value, as well as the spin moment, is clearly below the calculated values determined using the LDA +  $U$ . The moments deduced using the GGA seem to be more accurate, which is in agreement with the results of valence band photoelectron spectroscopy. The total spin magnetic moment of XMCD amounts to  $2.40\mu_B$  per formula unit  $Mn_2CoSn$ , which fits very well with the magnetic moment of  $2.59\mu_B$  determined by SQUID magnetometry. The difference is attributed to difficulties using the sum rule analysis for Mn. The spin-orbit splitting is relatively small compared to Co atoms, and the broad peaks due to overlap of Mn atoms with magnetic moments of opposite sign complicate analysis. The superposed part between the  $L_3$  and  $L_2$  edges in XMCD reduces the individual values of the integration in the spin sum rule. The determined value of  $1.68\mu_B$  for the partial magnetic moment of Mn atoms per formula unit may thus probably be higher in reality.

## V. SUMMARY AND CONCLUSION

In conclusion we have presented a comprehensive study of the cubic Heusler ferrimagnet  $Mn_2CoSn$ .  $Mn_2$ -based Heusler compounds occur in cubic and tetragonal modifications and have prospective properties for spintronics applications, and in particular for the growing field of spin transfer torque. For  $Mn_2CoSn$ , theoretical considerations suggested two possible ground states in the ordered inverse cubic Heusler structure, a half-metallic ferrimagnet and a metallic ferrimagnet. An L2<sub>1b</sub>-type disorder between Co and Mn I atoms in  $Mn_2CoSn$  was shown by Mössbauer and NMR studies as well as valence band hard x-ray photoelectron spectroscopy. Electronic structure calculations incorporating this type of disorder proposed a nearly half-metallic ferrimagnetic ground state with a high spin polarization for  $Mn_2CoSn$ . The magnetic moments determined using SQUID magnetometry and XMCD are within the range of the Slater-Pauling value ( $3\mu_B$ ) corroborating the theory of a nearly half-metallic ferromagnetic ground state. The high TC (598 K) facilitates room-temperature and above application. Future work should be directed toward improvement of the synthetic method in order to remove or reduce the impurity content and the experimental investigation of the assumed high spin polarization.

## Acknowledgements

This work was financially supported by the Deutsche Forschungsgemeinschaft (DfG), Projects No. TP 1.2-A and No. TP 1.3-A of research unit FOR 1464 Advanced Spintronic Materials and Transport Phenomena (ASPIMATT), as well as Projects No. P1 and No. P7 of research unit FOR 559, and by Stiftung Innovation, Rheinland-Pfalz.

This work was partially supported by the Nanotechnology Network Project, the Ministry of Education, Culture, Sports, Science, and Technology (MEXT), Japan. The authors are grateful to HiSOR, Hiroshima University, and JAEA/SPring-8 for the development of the HXPS experimental station at BL15XU of SPring-8. G.L. acknowledges the support by the Institute of Physics, Chinese Academy of Sciences (Beijing), and a fellowship by the Alexander von Humboldt Stiftung. The HAXPES and XMCD measurements were performed under the approval of NIMS (Proposal No. 2008A4905) and JASRI (Proposals No. 2008A0017 and No. 2008A1606). The authors thank the entire staff of SPring-8 for assistance. Work at ALS/LBNL was supported by the Director, Office of Science, Office of Basic Energy Sciences, of the U.S. DOE (Contract No. DE-AC02-05CH11231).

### Bibliography

1. F. Heusler, *Verh. d. DPG* 5, 219 (1903).
2. Y. Sakuraba, M. Hattori, M. Oogane, Y. Ando, H. Kato, A. Sakuma, T. Miyazaki, and H. Kubota, *Appl. Phys. Lett.* 88, 192508 (2006).
3. B. Balke, G. H. Fecher, H. C. Kandpal, C. Felser, K. Kobayashi, E. Ikenaga, J. J. Kim, and S. Ueda, *Phys. Rev. B* 74, 104405 (2006).
4. S. A. Wolf, D. D. Awschalom, R. A. Buhrman, J. M. Daughton, S. Molnar, M. L. Roukes, A. Y. Chtchelkanova, and D. M. Treger, *Science* 294, 1488 (2001).
5. M. Ishikawa, J. L. Jorda, and A. Junod, *Superconductivity in d- and f-Band Metals 1982* (W. Buckel and W. Weber, Kernforschungszentrum Karlsruhe, Germany, 1982).
6. J. Winterlik, G. H. Fecher, C. Felser, M. Jourdan, K. Grube, F. Hardy, H. von Löhneysen, K. L. Holman, and R. J. Cava, *Phys. Rev. B* 78, 184506 (2008).
7. J. Winterlik, G. H. Fecher, A. Thomas, and C. Felser, *Phys. Rev. B* 79, 064508 (2009).
8. R. Tickle and R. D. James, *J. Magn. Magn. Mater.* 195, 627 (1999).
9. Y. Sutou, Y. Imano, N. Koeda, T. Omori, R. Kainuma, K. Ishida, and K. Oikawa, *Appl. Phys. Lett.* 85, 4358 (2004).
10. A. Planes, Ll. Mañosa, and M. Acet, *J. Phys. Condens. Matter* 21, 233201 (2009).
11. P. J. Shamberger and F. S. Ohuchi, *Phys. Rev. B* 79, 144407 (2009).
12. T. Graf, P. Klaer, J. Barth, B. Balke, H.-J. Elmers, and C. Felser, *Scr. Mater.* 63, 1216 (2010).
13. D. P. Young, P. Khalifah, R. J. Cava, and A. P. Ramirez, *J. Appl. Phys.* 87, 317 (2000).
14. D. P. Oxley, R. S. Tebble, C. T. Slack, and K. C. Williams, *Nature (London)* 194, 465 (1962).

15. B. Balke, G. H. Fecher, J. Winterlik, and C. Felser, *Appl. Phys. Lett.* 90, 152504 (2007).
16. J. Winterlik, B. Balke, G. H. Fecher, C. Felser, M. C. M. Alves, F. Bernardi, and J. Morais, *Phys. Rev. B* 77, 054406 (2008).
17. S. Wurmehl, H. C. Kandpal, G. H. Fecher, and C. Felser, *J. Phys. Condens. Matter* 18, 6171 (2006).
18. J. C. Slonczewski, *J. Magn. Magn. Mater.* 159, L1 (1996).
19. A. Kalitsov, M. Chshiev, I. Theodonis, N. Kioussis, and W. H. Butler, *Phys. Rev. B* 79, 174416 (2009).
20. H. Kurt, K. Rode, M. Venkatesan, P. S. Stamenov, and J. M. D. Coey, *Phys. Rev. B* 83, 020405 (2011).
21. G.D.Liu, X.F.Dai, S.Y.Yu, Z.Y.Zhu, J.L.Chen, G.H.Wu, H. Zhu, and J. Q. Xiao, *Phys. Rev. B* 74, 054435 (2006).
22. S. R. Barman, S. Banik, A. K. Shukla, C. Kama, and A. Chakrabarti, *Europhys. Lett.* 80, 57002 (2007).
23. S. Chadov, G. H. Fecher, C. Felser, J. Minar, J. Braun, and H. Ebert, *J. Phys. D* 42, 084002 (2009).
24. V. V. Surikov, V. N. Zhordochkin, and T. Y. Astakhova, *Hyperfine Interact.* 59, 469 (1990).
25. N. Lakshmi, A. Pandey, and K. Venugopalan, *Bull. Mater. Sci.* 25, 309 (2002).
26. N. Lakshmi, R. K. Sharma, and K. Venugopalan, *Hyperfine Interact.* 160, 227 (2005).
27. G. D. Liu, X. F. Dai, H. Y. Liu, J. L. Chen, Y. X. Li, G. Xiao, and G. H. Wu, *Phys. Rev. B* 77, 014424 (2008).
28. J. Schaf, K. L. Dang, P. Veillet, and I. A. Campbell, *J. Phys. F* 13, 1311 (1983).
29. T. Nakamura, T. Muro, F. Z. Guo, T. Matsushita, T. Wakita, T. Hirono, Y. Takeuchi, and K. Kobayashi, *J. Electron Spectrosc. Relat. Phenom.* 144-147, 1035 (2005).
30. Y. Saitoh, H. Kimura, Y. Suzuki, T. Nakatani, T. Matsushita, T. Muro, T. Miyahara, M. Fujisawa, K. Soda, S. Ueda, A. Sekiyama, S. Imada, and S. Suga, *Nucl. Instrum. Methods A* 467-468, 553 (2001).
31. K. Lagarec and D. G. Rancourt, *Nucl. Instrum. Methods Phys. Res., Sect. B* 129, 266 (1997).
32. S. Nadolski, M. Wojcik, E. Jedryka, and K. Nesteruk, *J. Magn. Magn. Mater.* 140, 2187 (1995).
33. P. Blaha, K. Schwarz, G. K. H. Madsen, D. Kvasnicka, and J. Luitz, WIEN2k, An Augmented Plane Wave + Local Orbitals Program for Calculating Crystal Properties (Karlheinz Schwarz, Techn. Universitaet Wien, Wien, Austria, 2001).
34. J. P. Perdew, K. Burke, and M. Ernzerhof, *Phys. Rev. Lett.* 77, 3865 (1996).
35. H. C. Kandpal, G. H. Fecher, C. Felser, and G. Schönhense, *Phys. Rev. B* 73, 094422 (2006).
36. V. I. Anisimov, F. Aryasetiawan, and A. I. Lichtenstein, *J. Phys. Condens. Matter* 9, 767 (1997).

37. V. I. Anisimov, I. V. Solovyev, M. A. Korotin, N. T. Czyzyk, and G. A. Sawatzky, *Phys. Rev. B* 48, 16929 (1993).
38. H. Ebert, in *Electronic Structure and Physical Properties of Solids. The Use of the LMTO Method*, Lecture Notes in Physics, Vol. 535, edited by H. Dreyse (Springer-Verlag, Berlin, Heidelberg, 1999), p. 191.
39. H. Ebert, The Munich SPR-KKR Package, Version 3.6, 2005, [<http://olymp.cup.uni-muenchen.de/ak/ebert/SPRKKR>].
40. H. Ebert, J. Minar, and V. Popescu, in *Band-Ferromagnetism*, Lecture Notes in Physics, Vol. 580, edited by K. Baberschke, M. Donath, and W. Nolting (Springer-Verlag, Berlin, Heidelberg, 2001), p. 371.
41. H. Nowotny and K. Schubert, *Z. Metallkd.* 37, 17 (1946).
42. A. Coelho, TOPAS ACADEMIC, Version 4.1, 2007.
43. M. Meinert, J.-M. Schmalhorst, and G. Reiss, *J. Phys. Condens. Matter* 23, 116005 (2011).
44. R. B. Helmholtz and K. H. J. Buschow, *J. Less-Common Met.* 128, 167 (1987).
45. P. J. Brown, T. Kanomata, K. Neumann, K. U. Neumann, B. Oulad-diaf, A. Sheikh, and K. R. A. Ziebeck, *J. Phys. Condens. Matter* 22, 506001 (2010).
46. C. S. Fadley, D. A. Shirley, A. J. Freeman, P. S. Bagus, and J. V. Mallow, *Phys. Rev. Lett.* 23, 1397 (1969).
47. S. Ouardi, B. Balke, A. Gloskovskii, G. H. Fecher, C. Felser, G. Schönhense, T. Ishikawa, T. Uemura, M. Yamamoto, H. Sukegawa, W. Wang, K. Inomata, Y. Yamashita, H. Yoshikawa, S. Ueda, and K. Kobayashi, *J. Phys. D* 42, 084010 (2009).
48. H. J. Elmers, G. H. Fecher, D. Valdaitsev, S. A. Nepijko, A. Gloskovskii, G. Jakob, G. Schönhense, S. Wurmehl, T. Block, C. Felser, P.-C. Hsu, W.-L. Tsai, and S. Cramm, *Phys. Rev. B* 67, 104412 (2003).
49. M. Kallmayer, H.C. Schneider, G. Jakob, H. J. Elmers, B. Balke, and S. Cramm, *J. Phys. D* 40, 1552 (2007).

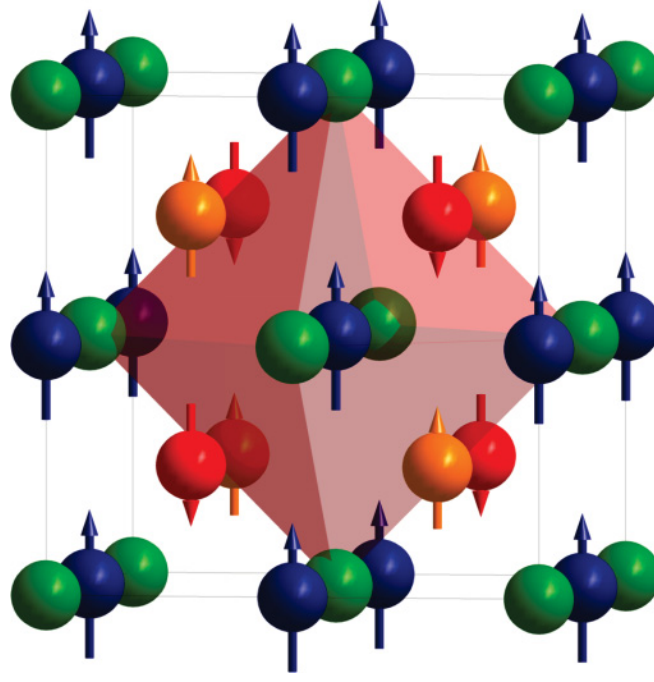


FIG. 1. (Color online) Cubic unit cell of ordered  $\text{Mn}_2\text{CoSn}$  with three different magnetic sublattices (space group 216,  $F\bar{4}3m$ ). Octahedrally coordinated Mn atoms with highly localized magnetic moments are in blue and couple antiferromagnetically to the red Mn atoms in the tetrahedral environment. The orange Co atoms are oriented parallel to the blue Mn atoms as postulated by the electronic structure calculations; the Sn atoms are green. It should be noted that the experiments hint at disorder between the red Mn atoms and the Co atoms.

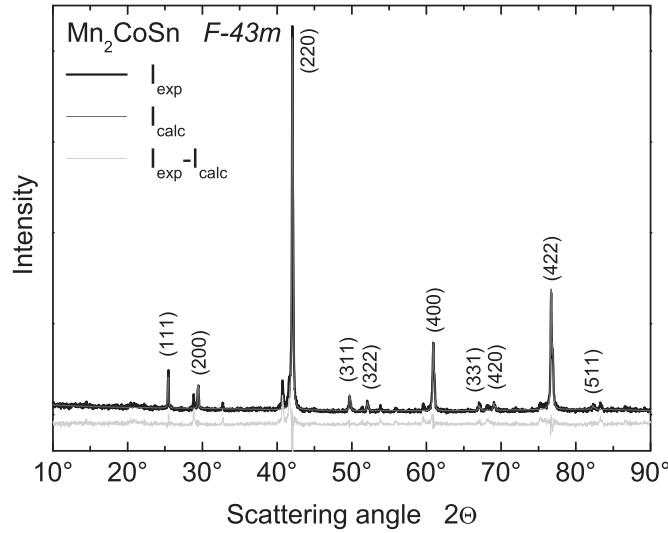


FIG. 2. Powder XRD and Rietveld refinement of  $\text{Mn}_2\text{CoSn}$ . The diffraction pattern was measured at room temperature using  $\text{Cu K}\alpha$  radiation. The black line corresponds to the experimental intensity, the red one to the refinement, and the gray one to the difference between experiment and refinement.

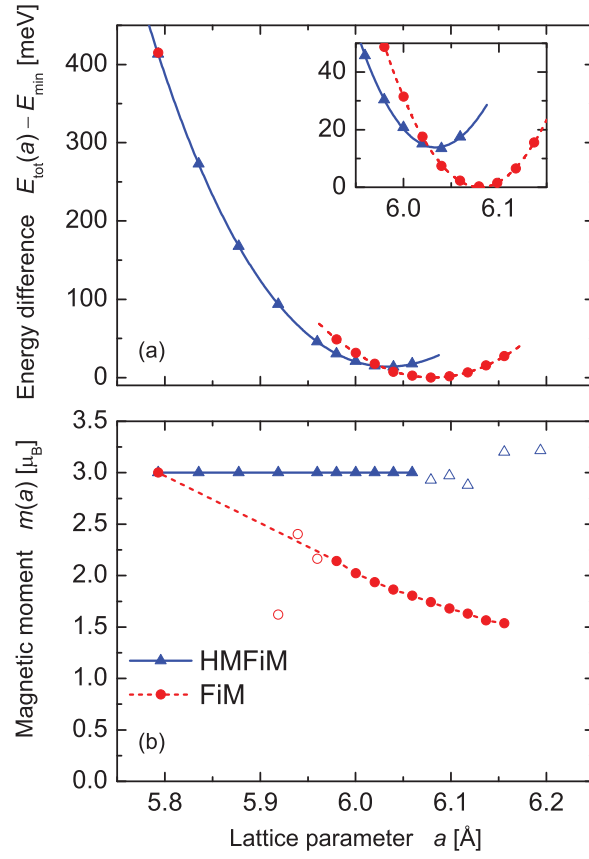


FIG. 3. (Color online) Optimization of the lattice parameter of  $\text{Mn}_2\text{CoSn}$ . (a) The difference in the total energies as a function of the lattice parameter. Only fully converged values are shown (see text). (b) The corresponding total magnetic spin moments. Open circles assign values where the calculation converged only conditionally; that is, energy convergence was reached but not charge convergence. The calculations were performed using WIEN2K

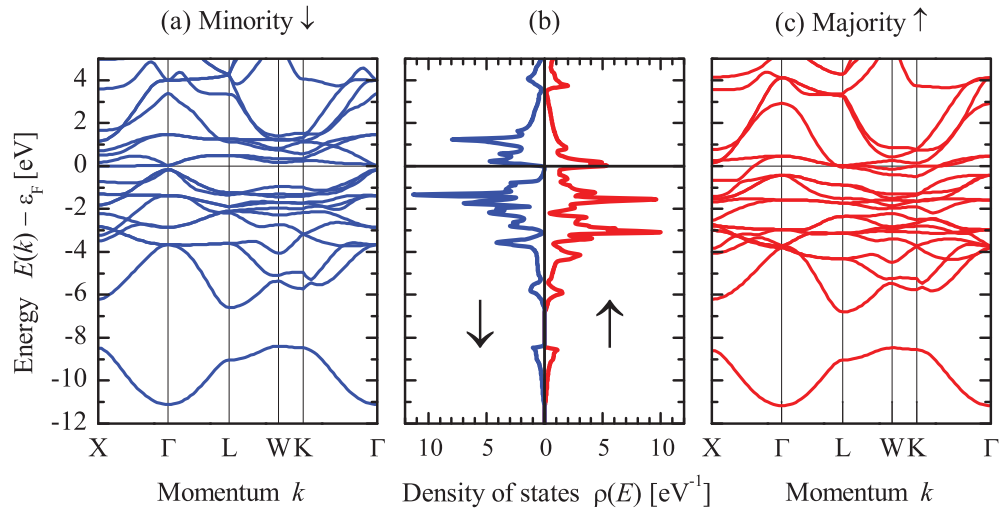


FIG. 4. (Color online) Electronic structure of half-metallic ferrimagnetic  $\text{Mn}_2\text{CoSn}$ . The spin-resolved band structure and density of states was calculated for the  $X_a$  structure with relaxed lattice parameter using WIEN2K with GGA.



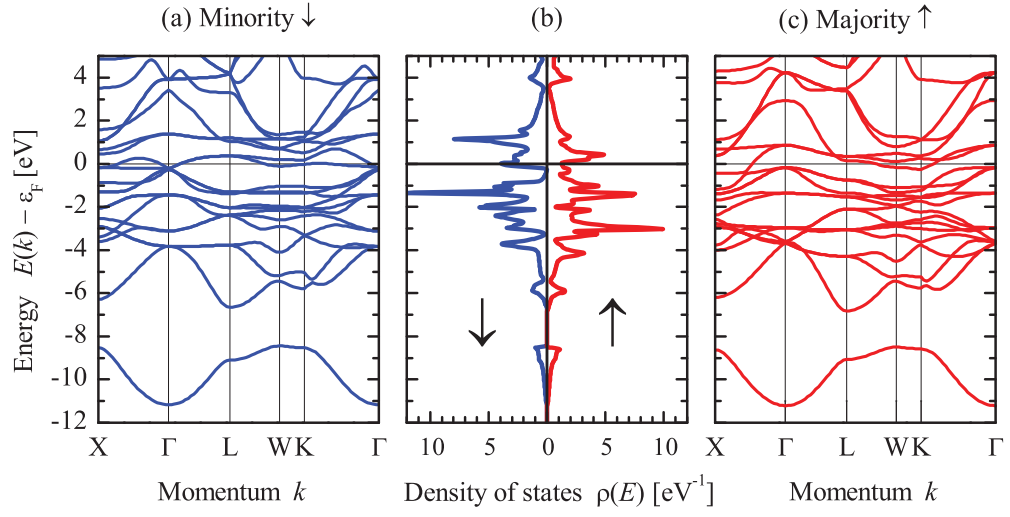


FIG. 5. (Color online) Electronic structure of regular ferrimagnetic  $\text{Mn}_2\text{CoSn}$ . The spin-resolved band structure and density of states was calculated for the  $X_a$  structure with relaxed lattice parameter using WIEN2K with GGA.

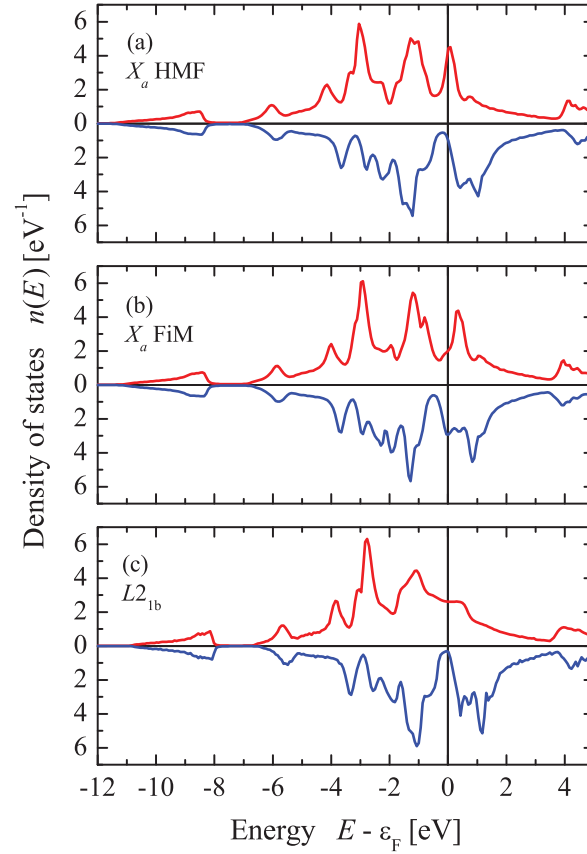


FIG. 6. (Color online) Structural dependence of the electronic structure of  $\text{Mn}_2\text{CoSn}$ . The spin-resolved density of states was calculated using SPR-KKR with GGA.

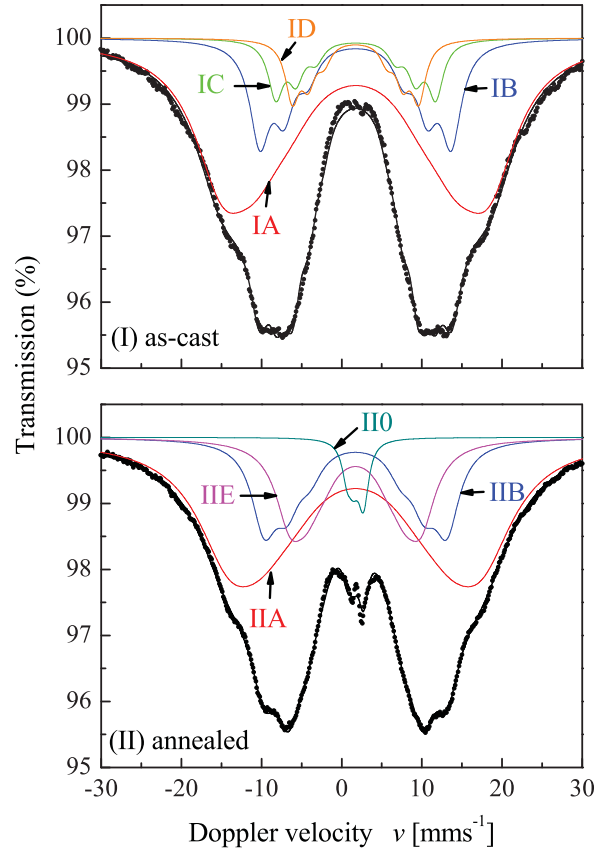


FIG. 7. (Color online) Mössbauer spectra of  $\text{Mn}_2\text{CoSn}$ . (I) The spectrum of an as-cast sample. (II) The spectrum of a sample after annealing for 14 days at a temperature of 1073 K and quenching afterward. The spectra were recorded at 225 K. The subspectra mentioned in the text are marked with arrows.

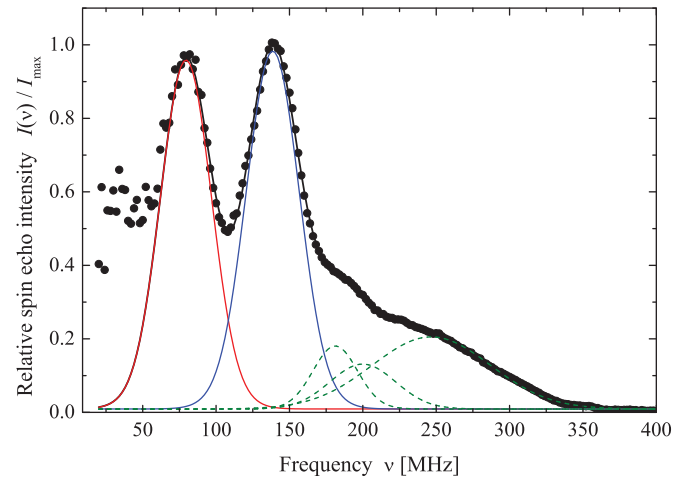


FIG. 8. (Color online) NMR of  $\text{Mn}_2\text{CoSn}$ . Displayed is the NMR spectrum taken at  $T = 4.2$  K after correction of the enhancement factor and  $\nu^2$  dependence. Lines are the result of a fit to Gaussians.

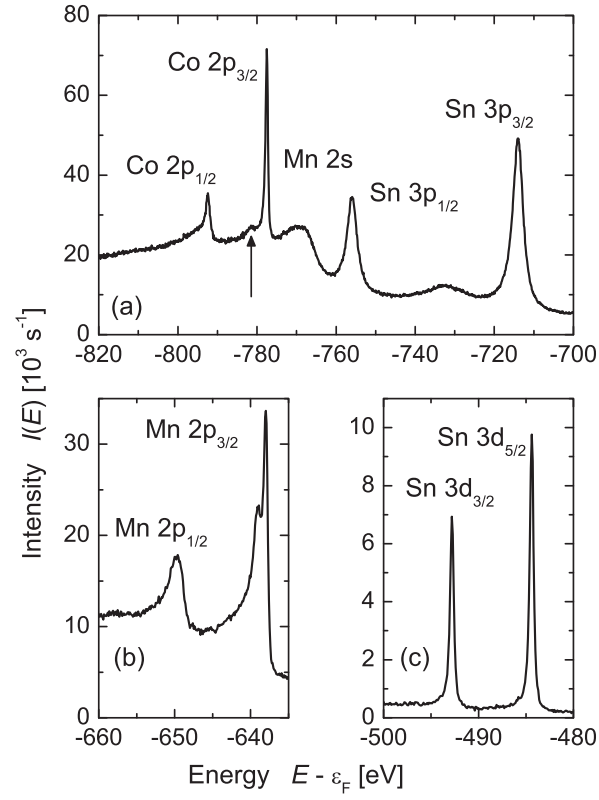


FIG. 9. Core-level photoemission of  $\text{Mn}_2\text{CoSn}$ . (a) The region of the Co 2p and Sn 3p states. (b) The 2p states of Mn. (c) The Sn 3d states. The measurements were performed at  $T = 300$  K sample temperature and 5.9534 keV photon energy. The arrow in (a) marks the 3.5 eV satellite of the Co 2p<sub>3/2</sub> excitation.

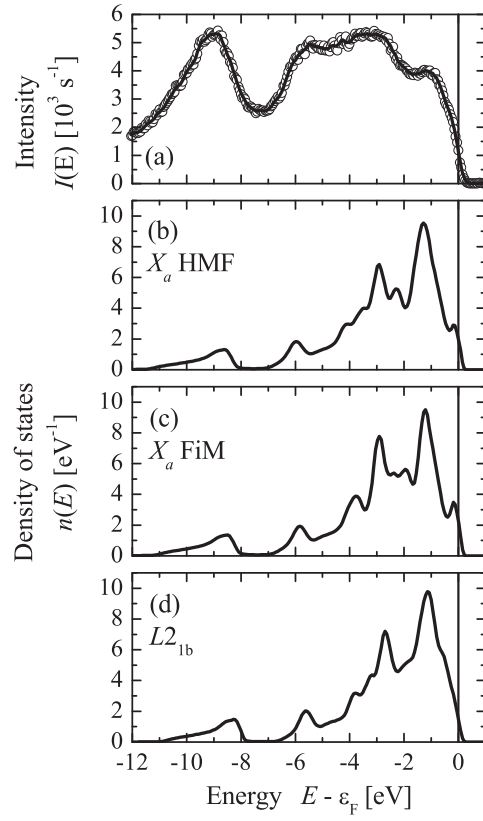


FIG. 10. Valence band photoemission and densities of states of  $\text{Mn}_2\text{CoSn}$ . (a) The valence band spectrum excited by  $h\nu = 5.94677$  keV photons. (b) to (d) The calculated densities of states for the different magnetic states of the  $X_a$  structure compared to the  $L2_{1b}$  structure. The measurements (a) were performed at  $T = 300$  K. In (b) to (d), the density of states is convoluted by a Fermi-Dirac distribution and smoothed by Gaussians to reflect the finite temperature and resolution of the photoemission experiment.

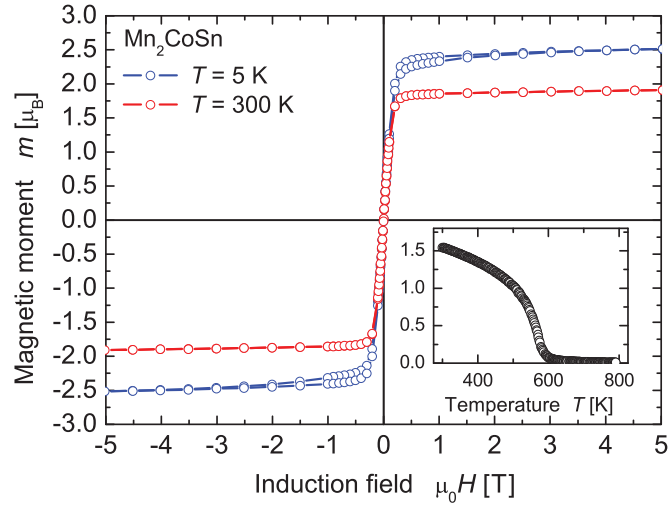


FIG. 11. (Color online) Magnetic properties of  $\text{Mn}_2\text{CoSn}$ . Displayed are the hysteresis loops measured at  $T = 5$  K and  $T = 300$  K. The inset shows the magnetic moment as a function of temperature between 300 and 800 K. The temperature-dependent curve was recorded at an induction field of  $\mu_0H = 1$  T.

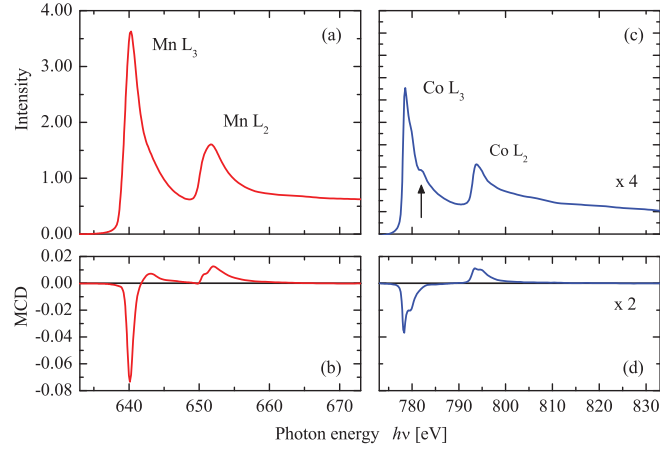


FIG. 12. (Color online) XMCD of  $\text{Mn}_2\text{CoSn}$ . Shown are the absorption spectra (a), (c) after background subtraction and the XMCD signals (b), (d) taken at the  $L_{3,2}$  edges of Mn (a), (b) and Co (c), (d). The spectra were taken at  $T = 15$  K using an induction field of  $\mu_0 H = 1.9$  T. Note that the intensity and XMCD of Co are multiplied by factors of 4 and 2, respectively.

TABLE I. Spin magnetic moments of  $\text{Mn}_2\text{CoSn}$  calculated using WIEN2K and the optimized lattice parameter of the half-metallic (HMF) or ferrimagnetic (FiM) state (all values are in  $\mu_B$ ). Mn I is on Wyckoff position  $4c$ , Co on  $4d$ , and Mn II on  $4b$ . Note: The total spin moment includes contributions of the interstitial as well as the induced moment at the Sn atoms.

	HMF		FiM	
	GGA	LDA + $U$	GGA	LDA + $U$
Co	1.17	1.54	0.96	1.57
Mn I	-1.39	-1.75	-2.49	-3.13
Mn II	3.21	3.25	3.24	3.69
Total	3.00	3.00	1.74	2.15

TABLE II. Spin magnetic moments of  $\text{Mn}_2\text{CoSn}$  calculated using SPR-KKR. The calculations were performed for different lattice parameters. All values of the magnetic moments are given in  $\mu_B$ .

	$a$ ( $\text{\AA}$ )	$m_{\text{tot}}$	$m_{\text{MnI}}$	$m_{\text{MnII}}$	$m_{\text{Co}}$
$X_a$	5.95	3.00	-0.83	3.03	0.81
$X_a$	6.05	1.45	-2.35	3.26	0.54
$L2_{1b}$	6.057	2.98	-1.23	3.24	0.99

TABLE III. Results of the deconvolution of the annealed sample II of  $\text{Mn}_2\text{CoSn}$ .

Atom	Resonance Frequency (MHz)	Rel. Intensity (%)	Gaussian Linewidth (MHz)
Co	138.6	37.2	18
Mn I	79.4	34.9	17
Mn II	181	5.5	15
Mn II	200	5.7	22
Mn II	246	16.7	40

TABLE IV. Spin-orbit splittings of the core levels of  $\text{Mn}_2\text{CoSn}$ . The value for Mn  $2p$  is averaged over the multiplet splitting. (All values are in eV; the HAXPES measurements were performed using  $h\nu = 5.9534$  keV with the resolution set to 250 meV.)

	Experiment		Calculation	
	HAXPES	XAS	WIEN2K	SPR-KKR
Mn $2p$	11.4	11.4	10.4	10.4
Co $2p$	15.0	15.2	14.8	14.8
Sn $3p$	42.0		42.1	42.1
Sn $3d$	8.4		8.7	8.7

TABLE V. Partial magnetic moments of  $\text{Mn}_2\text{CoSn}$ . Compared are the spin moments determined from the XMCD measurements to the SQUID magnetic moment and the calculated values in the half-metallic (HMF) and ferrimagnetic (FiM) states and the disordered  $L2_{1b}$  structure using SPR-KKR. (The value for Mn corresponds to the total spin moment of Mn in the primitive cell  $\text{Mn}_2\text{CoSn}$ , i.e., the value of two Mn atoms. All values are in  $\mu_B$ .)

	XMCD	SQUID	HMF	FiM	$L2_{1b}$
Co	0.72		0.81	0.54	0.99
Mn	1.68		2.19	0.91	1.99
Total	2.40	2.59	3.00	1.45	2.98